

Final Draft
of the original manuscript:

Doenges, B.; Istomin, K.; Soeker, M.; Schell, N.; Krupp, U.; Pietsch, U.;
Fritzen, C.-P.; Christ, H.-J.:

**Experimental investigation and numerical description of the
damage evolution in a duplex stainless steel subjected to
VHCF-loading**

In: Materials Science and Engineering A (2015) Elsevier

DOI: 10.1016/j.msea.2015.08.021

Experimental investigation and numerical description of the damage evolution in a duplex stainless steel subjected to VHCF-loading

B. Dönges^{a,b}, K. Istomin^c, M. Söker^d, N. Schell^e, U. Krupp^d, U. Pietsch^c, C.-P. Fritzen^b, H.-J. Christ^a

^a*Institut für Werkstofftechnik, Universität Siegen, D-57068 Siegen, Germany*

^b*Institut für Mechanik und Regelungstechnik – Mechatronik, Universität Siegen, D-57068 Siegen, Germany*

^c*Festkörperphysik, Universität Siegen, D-57068 Siegen, Germany*

^d*Fakultät für Ingenieurwissenschaften und Informatik, Hochschule Osnabrück, D-49009 Osnabrück, Germany*

^e*Helmholtz-Zentrum Geesthacht, Zentrum für Material- und Küstenforschung, D-21502 Geesthacht, Germany*

Keywords: Very high cycle fatigue; fatigue crack initiation; short fatigue crack propagation; high energy x-ray diffraction; mesoscopic simulation

Corresponding author: Benjamin Dönges, e-mail: benjamin.doenges@uni-siegen.de

ABSTRACT

The present study documents how the irreversible fraction of cyclic plastic strain, induced by loading amplitudes close to the durability limit, causes fatigue damage such as (i) slip band development, (ii) fatigue crack initiation and (iii) short fatigue crack propagation. The damage evolution of the austenitic-ferritic duplex stainless steel X2CrNiMoN22-5-3 (318 LN) was investigated up to one billion load cycles by means of high resolution electron microscopy (HR-SEM, TEM), focused ion beam (FIB) cutting, confocal laser scanning microscopy (CLSM), *in-situ* far field microscopy and high-energy (87.1 keV) X-ray diffraction (XRD) experiments. The experimentally identified damage mechanisms were implemented into three-dimensional finite element simulations, which consider crystal plasticity. These simulations enable fatigue life predictions of real microstructures obtained for instance by means of, e.g. automated electron back scatter diffraction (EBSD) analysis. The simulations allow for determining whether microcracks (i) initiate in a microstructure, (ii) arrest in the midst of the first grain, (iii) are permanently, (iv) temporary or (v) not at all blocked by grain or phase boundaries. Moreover, this concept is capable to contribute to the concept of tailored microstructures for improved cyclic-loading behaviour.

1. Introduction

Austenitic-ferritic duplex stainless steels are characterized by high corrosion resistance, weldability and relatively high strength. These properties make them very attractive for applications such as off-shore systems or systems for the chemical and petrochemical industry. Frequently, such applications are connected with cyclic loading at high frequencies and during long periods of operation, respectively, causing very high numbers of load cycles ($N > 10^7$).

Classical engineering-concepts for dimensioning of dynamically high-loaded components imply mathematical approaches based on experimentally obtained fatigue data (S-N-/Wöhler-diagrams) and the assumption that below a certain load amplitude no cycle-dependent damage occurs. In the case of bcc carbon steels it is widely accepted that a fatigue limit exists and that after 10^7 load cycles no fracture will take place. In the case of fcc materials, such as aluminum or copper alloys, a fatigue limit is often not found. Their higher packing density causes a much lower critical shear stress for dislocation motion and hence, fatigue damage evolves. However, in most practical cases the conventional fatigue-limit concept is applied for nearly all engineering metallic materials that experience more than 10^7 cycles during service.

In contrast to the former assumptions, recent fatigue experiments have proven that even bcc materials may fail after many ten millions of load cycles due to crack initiation from internal inclusions [1, 2]. On the other hand, fcc materials can exhibit a fatigue limit caused by formation [3] or existence [4] of a second phase. In the absence of inclusions of a critical size, fatigue damage in form of slip band generation occurs at the surface caused by slip irreversibility. According to Tanaka and Mura [5], slip irreversibility eventually causes initiation and propagation of microstructurally short fatigue cracks. This kind of slip irreversibility can be attributed to vacancy-type annihilation of dislocations moving back and forth on neighboring slip planes during cyclic loading [6]. If the applied stress amplitude is not sufficient to make one of these crack nuclei overcome the adjacent grain or phase boundary, the conventional fatigue limit is reached. As long as irreversible dislocation motion is not completely eliminated, the accumulation of plastic slip may take place at least locally and, hence, fatigue failures at very high numbers of cycles ($N_f > 10^7$) may occur. Thus, the physical fatigue limit can be considered as an irreversibility limit.

In the case of two-phase materials, which contain both lattice structures, the fatigue behaviour cannot be derived from the respective behaviour of the single phases only. Under loading conditions close to the fatigue limit, the process of fatigue crack initiation and short fatigue crack propagation can represent up to 90% of the number of load cycles until failure (N_f) and cannot be described by means of classical fracture mechanics concepts, such as the linear elastic fracture mechanics (LEFM). The phases of fatigue crack initiation and short fatigue crack propagation are strongly affected by microstructural properties, such as the grain size and the presence of phase boundaries. Phase boundaries can significantly influence the fatigue behaviour by blocking an initiating damage development in form of slip bands or microcracks.

Different experimental methods were applied in this study in order to characterize the fatigue damage evolution in form of (i) slip band development, (ii) fatigue crack initiation and (iii) early fatigue crack propagation under loading conditions close to the fatigue limit up to one billion load cycles. Furthermore, in order to numerically describe the mechanisms of fatigue crack initiation and short fatigue crack propagation, a three-dimensional model was developed, which considers the available slip systems (e.g. obtained by means of EBSD) in the microstructure and the barrier effect of grain and phase boundaries. The solution of this problem was calculated numerically using the finite element program ABAQUS. In the following the experimental results obtained by means of ultrasonic fatigue testing in combination with analysis techniques such as high-energy X-ray diffraction, electron microscopy and optical microscopy as well as the modeling approach are presented.

2. Experimental details

Ultrasonic fatigue testing was applied to conduct symmetric push-pull fatigue experiments ($R = -1$) at room temperature in laboratory air in a reasonable testing time. To reach these high testing frequencies, an axially symmetric hourglass shaped sample is stimulated in the range of its longitudinal resonant frequency at around 20 kHz by means of an ultrasonic converter, which transfers a sinusoidal electric signal into a sinusoidal mechanical stress wave. This stress wave is magnified in its amplitude by means of a narrowing horn and transferred into the sample. The stress amplitude is maximum at the most narrow cross section (i.e., in the middle) of the sample. The elastic strain

amplitude is measured by means of a strain gage during calibration and is used to calculate the stress amplitude via Hooke's law. A control system (designed by Boku Vienna) keeps the stress amplitude constant during testing via online control of the signal of an inductive displacement gauge. The damping of the investigated duplex stainless steel causes a significant heat generation, which was counteracted by means of an air cooling system and a pulse-pause (100 ms / 1200 ms) loading mode. The latter reduced the effective testing frequency from around 20 kHz to about 1.5 kHz. This enables testing of one billion load cycles within nearly 7.5 days. To investigate the influence of the laboratory-air atmosphere, additional fatigue experiments were executed in vacuum ($p < 5 \cdot 10^{-6}$ mbar). Since cooling by pressurized air is inapplicable, the pulse to pause time were reduced during the vacuum tests (50 ms / 9900 ms). Hence, testing of one hundred million load cycles took around 11.5 days.

The investigated duplex stainless steel was delivered as hot-rolled and solution-annealed bars with a diameter of 25 mm. The as-received microstructure shows elongated grains along the rolling direction (sample axis) and consists of 50% austenite and 50% ferrite each. In order to facilitate the experimental investigations, grain coarsening by means of an additional heat treatment was executed at 1250°C for 4h. Subsequently, the material was cooled down linearly with time to 1050°C within 3h and afterwards quenched in water. During the annealing procedure, the original volume fraction of both phases was maintained and the mean grain diameters of austenite and ferrite were increased to 33 μm and to 46 μm , respectively (fig. 1). The hourglass shaped ultrasonic fatigue samples were produced by machining and subsequent mechanical grinding and electrolytical polishing. By means of a Hall-Petch analysis [7, 8], the frictional shear stresses for dislocation generation and motion were determined to be $\tau_{\text{H}}=68$ MPa for the austenite phase and $\tau_{\text{H}}=99$ MPa for the ferrite phase [9].

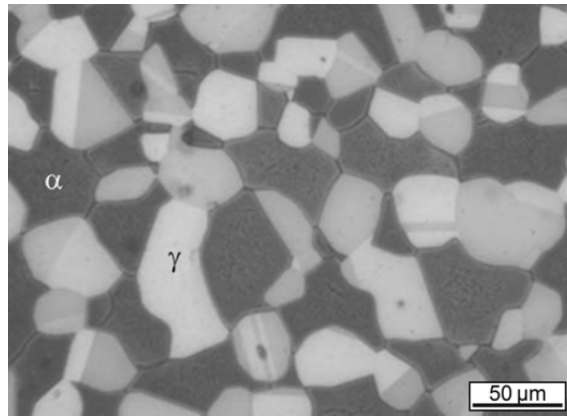


Fig. 1: Microstructure of the investigated duplex stainless steel perpendicular to the rolling direction after the heat treatment containing austenite (fcc, bright) and ferrite (bcc, dark) [4]

The crystallographic orientation and phase distributions were investigated by means of automated EBSD. The crystallographic data served as basis for the calculation of the Schmid factors and the favorable slip systems. Dislocation arrangements in the bulk material of run-out samples were investigated by means of electrolytically thinned TEM lamellae. Ultrasonic fatigue samples with shallow notches were examined during fatigue experiments by means of an optical far field microscope. The damage development concentrates in the shallow notch due to stress intensification and thus, fatigue crack initiation is most likely in this region of the sample. This enabled the *in-situ* investigation of fatigue crack initiation and short fatigue crack propagation.

The investigation of fracture surfaces, slip traces and crack initiation sites was executed by means of high resolution SEM. In order to obtain three dimensional information about slip traces and short fatigue cracks, cross sections perpendicular to the sample surface were investigated by means of SEM in combination with FIB-cutting.

X-ray diffraction measurements were performed at the P07 high energy materials science beamline of Helmholtz-Zentrum Geesthacht located at PETRA III storage ring at DESY (Hamburg, Germany) using a photon energy of 87.1 keV prior to the fatigue experiment as well as after 20, 100, 500 thousand and 1, 5, 10, 50, 100 million load cycles at a load amplitude of 380 MPa in laboratory air ($R = -1$). A rectangular X-ray beam (vertical: 150 μm , horizontal: 120 μm) was obtained using 2 pairs of slits. The vertical axis of the hourglass shaped sample was aligned parallel to the rotation axis of the

goniometer. The specimen was mounted to the ultrasonic fatigue testing equipment (UFTE) for fatigue loading. The frame of the UFTE was attached to the goniometer, so the whole installation could be rotated around its vertical axis. A fast read-out image plate 2D-detector (2048 x 2048 pixels) with the pixel size of 0.2 mm was placed 1.19 m behind the specimen. The high photon energy (absorption length 2.5 mm in steel) allowed for probing the whole sample in transmission mode. More information regarding the experimental set-up can be found in reference [10]. The incoming beam was focused close to the surface in the waist of the fatigue specimen. A finite element (FE) base motion analysis simulation was applied to confirm the value and location of the maximum von Mises stress amplitude (fig. 2) resulting from the resonance oscillation in the UFTE. After each fatigue interval, the UFTE was paused in order to conduct a series of diffraction scans, whilst the sample was rocked around its axis of rotation (angle Ψ) in the range of $\pm 10.0^\circ$ with steps of 0.2° . The exposure time for each shot was 1 s. The diffracted beam was registered using the 2D-detector, where detector frames were recorded as the function of the rotation angle Ψ and the number of load cycles.

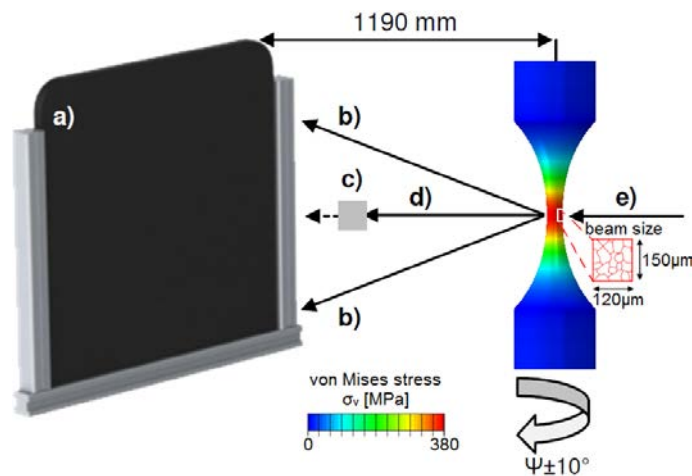


Fig. 2: Experimental set-up (schematically) and von Mises stress distribution in the hourglass-shaped ultrasonic fatigue sample according to a FE base motion analysis: (a) 2D-detector, (b) diffracted beam, (c) beam stop, (d) transmitted beam, (e) incident beam

3. Results and model assumptions

3.1 Phenomenological investigations

The results of numerous laboratory fatigue experiments showed that cracks in the investigated duplex stainless steel predominantly initiate at the sample surface. Only if there is an extraordinary large subsurface defect, cracks initiate from the inside of the sample. This was observed solely in the case of two fatigue samples in 130 and 300 Hz experiments [4]. Fatigue experiments in laboratory air atmosphere on electrolytically polished samples showed that surface cracks with a length of up to 120 μm initiate at and below the stress amplitude of $\Delta\sigma/2=340$ MPa. However, these cracks do not lead to material failure within 10^9 load cycles because of impeded crack propagation. Hence, the investigated duplex stainless steel seems to possess a real fatigue limit of about $\sigma_{\text{FL}}=340$ MPa. At 380 MPa two samples failed at very high numbers of load cycles ($N_f \approx 4 \cdot 10^7$ and $N_f \approx 10^8$) (see fig. 3).

Experiments with identical samples fatigued in vacuum ($p < 5 \cdot 10^{-6}$ mbar) showed an approximately 40 times higher fatigue life at identical stress amplitudes. This can be attributed to the virtually complete absence of environmental attack at the sample surface (fig. 3). During fatigue experiments in air, atmospheric components are adsorbed on the sample surface and possibly absorbed by the material. In areas of high plastic deformation, this may lead to a local embrittlement, which prevents a re-welding of freshly generated surface [11, 12]. In other words, the fraction of re-welding of freshly generated surface is much higher in vacuum. Hence, the irreversible fraction of the crack tip slide displacement is lower and leads to a slower crack propagation. Furthermore, the missing atmosphere at the sample surface causes a lower surface energy. This leads to a lower activation stress for dislocation sources as well as a higher mobility of dislocations [12, 13]. In the case of vacuum testing, the numbers of load cycles to failure were very close to the ultimate number of load cycles applied (here: 10^8). Hence, no sound conclusion can be drawn regarding the value of the vacuum fatigue limit.

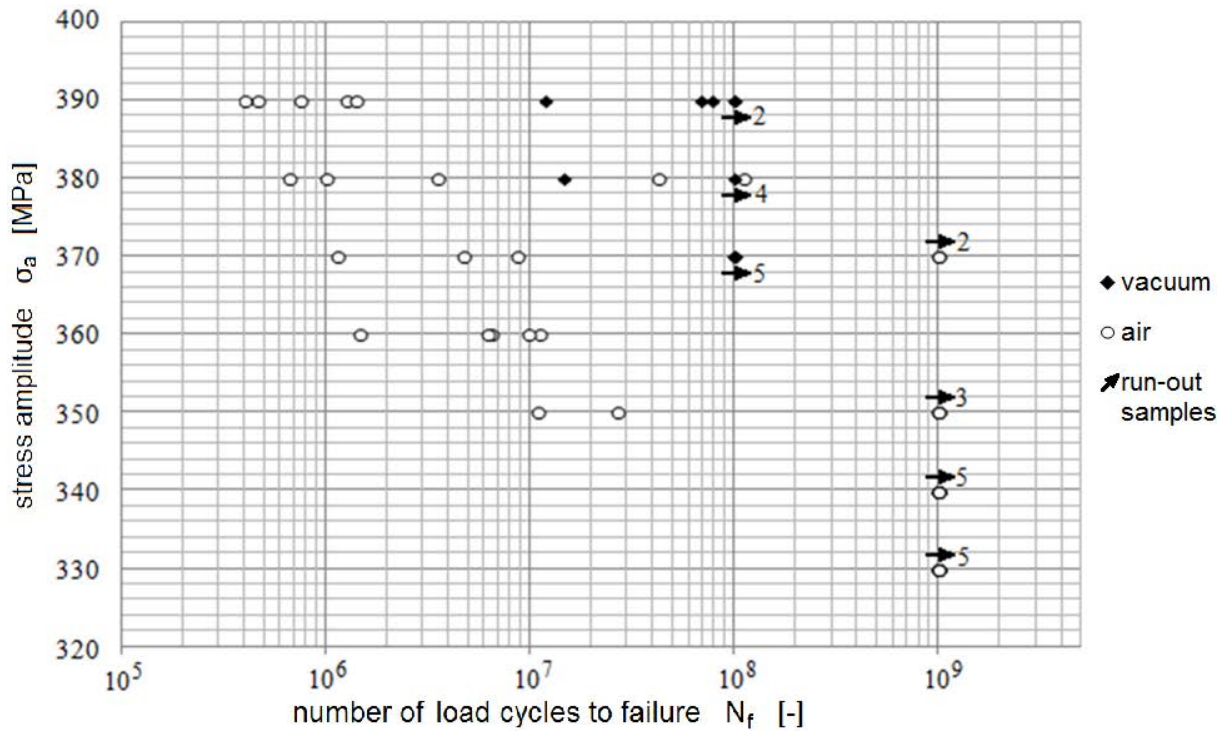


Fig. 3. S-N data of the investigated duplex stainless steel tested at 20 kHz

(open symbols: air-atmosphere-tests; full diamonds: vacuum-tests; arrows: run-out samples; the numbers beside the arrows indicate the number of tests performed)

3.2 Development of the irreversible fraction of cyclic plastic strain

The accumulated irreversible fraction of cyclic plastic shear strain, which is concentrated in slip bands, appears at the sample surface in form of slip traces (line of intersection between activated slip planes and surface plane). Slip traces predominantly consist of extrusions, which sometimes are accompanied by intrusions. The cyclic development of slip traces was investigated by means of CLSM (fig. 4). Based on the obtained topography data, the cyclic development of the height profile of an extrusion-intrusion-pair along the white dashed line in an austenite grain shown in figure 4f was analyzed (fig. 5). The roughness profile at different numbers of load cycles is presented in figure 5a, whereas the development of the height of an extrusion-intrusion pair h is presented as squares in figure 5b. The height increased until about 10^5 load cycles and subsequently increased only marginally until $5 \cdot 10^8$ load cycles. This reduction of the irreversible fraction of cyclic plastic shear strain indicates a relatively strong cyclic hardening of single austenite slip bands. The slip band density in the austenite grains increased until about 10^8 load cycles and subsequently remained almost constant until

$5 \cdot 10^8$ load cycles. Probably, the cyclic hardening in the activated austenite slip bands causes a shifting of plastic deformation into neighboring areas within the same grain. This development is quantified in figure 5b (stars) by means of the width w of a slip trace agglomeration along the white dashed line as shown in figure 4f. A transgranular microcrack with a length of about $5 \mu\text{m}$ initiated between $2 \cdot 10^4$ and 10^5 load cycles in a ferrite grain, starting from the intersection point between a phase boundary and a slip trace in a neighboring austenite grain (marked by an arrow in fig. 4b). The crack did not grow further until $5 \cdot 10^8$ load cycles, which was the ultimate number of load cycles for this experiment.

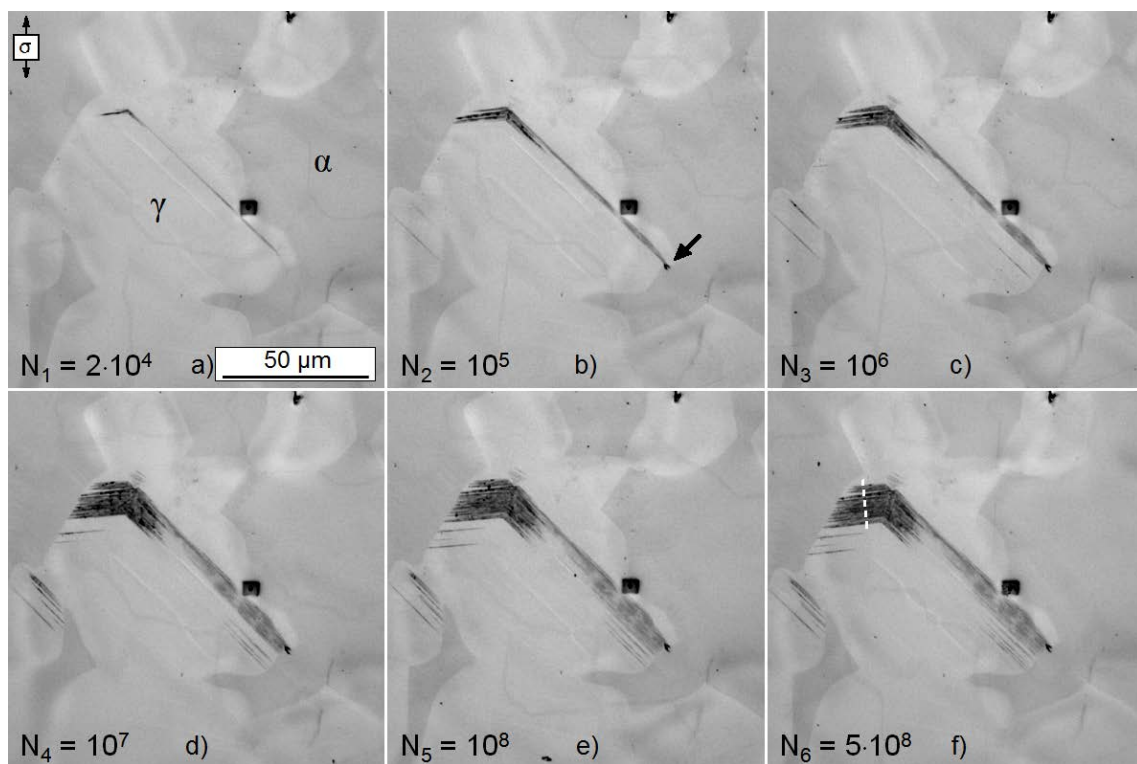


Fig. 4: (a-f) Cyclic development of slip traces in austenite grains (bright areas) and b) microcrack initiation in ferrite phase (dark areas), $\Delta\sigma/2 = 340 \text{ MPa}$

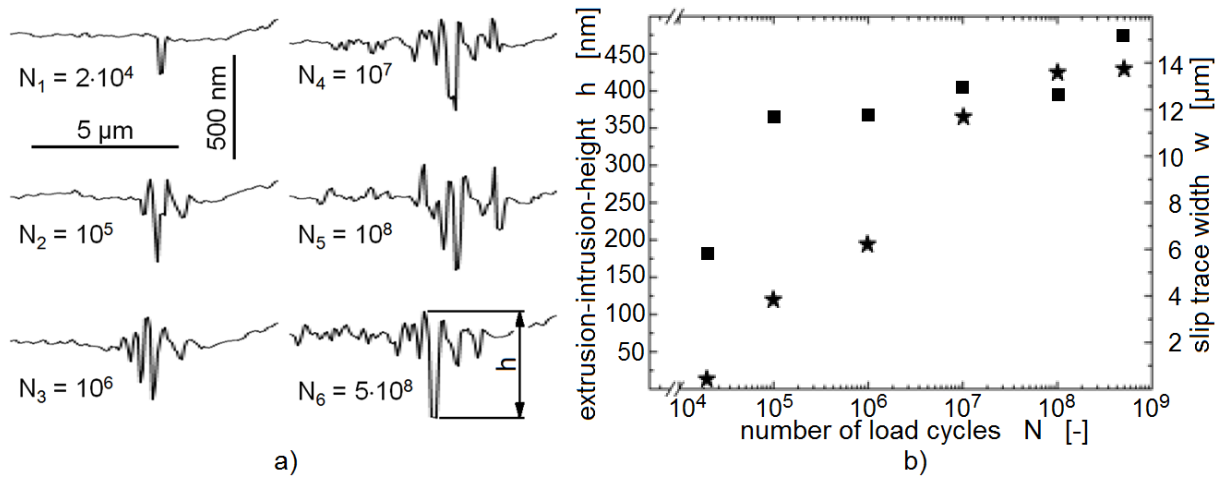


Fig. 5: (a) Development of the roughness profile with the number of loading cycles measured along the white dashed line in fig. 4f and (b) development of the height h of an extrusion-intrusion-pair (squares) and the width w of a slip trace (stars)

3.3 Microcrack initiation

Most frequently, the following three mechanisms of fatigue crack initiation were observed in the investigated duplex stainless steel: (i) transgranular initiation in ferrite grains (fig. 6a), (ii) intergranular initiation at phase boundaries due to very localized plastic deformation of adjacent ferrite grains (fig. 6b) and (iii) intergranular initiation at phase boundaries due to high grain boundary normal stresses without any plastic deformation of adjacent ferrite grains (fig. 6c). In all three cases, at phase boundaries impinging slip bands of neighboring austenite grains seem to provoke stress intensifications, which lead to fatigue crack initiation. The microstructure shown in figure 6a contains several microcracks which initiated transgranularly at a $\{112\} \langle 111 \rangle$ slip system in a ferrite grain starting from intersection points between a phase boundary and slip traces at a $\{111\} \langle 110 \rangle$ slip system in a neighboring austenite grain. Tanaka and Mura [5] assume that transgranular fatigue crack initiation can be attributed to local accumulation of dislocation dipoles caused by cyclic plastic shear strain. The dislocation dipoles increase the stored energy stepwise until a critical value is reached, at which crack initiation occurs after a number of load cycles N_i , according to

$$N_i \approx \frac{3\pi d^3 w_s (1 - \nu)}{2G[1 + 2\ln(\frac{4R}{d})]} \cdot \frac{1}{(\Delta\gamma_{pl})^2} \quad (1)$$

where G is the shear modulus, w_s is the specific fracture energy that is necessary to generate the fracture surface, ν is Poisson's ratio, d is the grain diameter, $\Delta\gamma_{pl}$ is the local plastic shear strain range and R is the outer cutoff radius of a stress field around a dislocation (fig. 6d). Chan [14] has extended this model by considering the cyclic irreversibility λ , the half crack length at crack initiation a and the slip band width h (Eq. 2). Equation 2 is valid for the case of a dislocation pile-up against a single grain boundary, too. For the cyclic irreversibility, Chan assumes a constant value of $\lambda = 0.005$.

$$N_i = \frac{9\pi h^2 a d (1 - \nu)}{2\lambda} \cdot \frac{1}{(\Delta\gamma_{pl})^2} \quad (2)$$

In the microstructure shown in figure 6b, an intergranular fatigue crack was developed due to the coalescence of several transgranularly initiated microcracks (compare with figs. 6d and e). Figure 6c shows an intergranular fatigue crack initiation at the phase boundary between the grains γ_1 and α_1 as well as α_2 due to high grain boundary normal stresses caused by impinging slip bands in a neighboring austenite grain according to the EGM-model [15] for fatigue crack initiation (fig. 6f).

Figure 7a shows the surface of an ultrasonic fatigue sample after one billion load cycles at the stress amplitude of 380 MPa. Only one austenite grain in the presented microstructure contains clearly visible slip traces (marked by a circle). Figure 7b shows this grain and a neighboring ferrite grain at higher magnification.

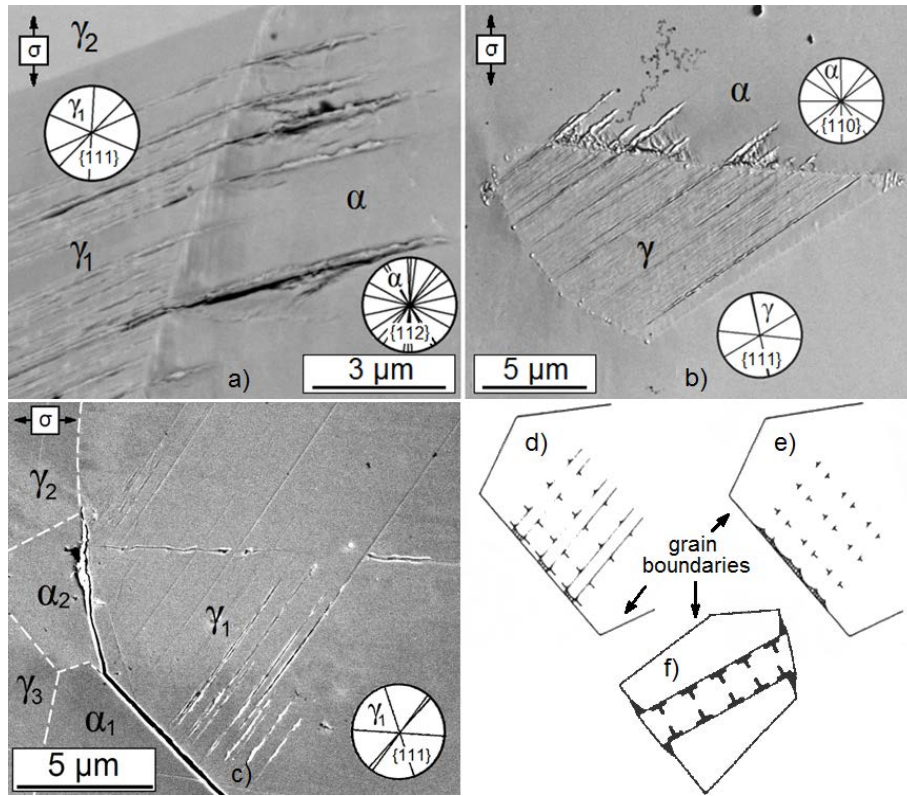


Fig. 6: (a) Trans- and (b) intergranular fatigue crack initiation at ferrite slip bands, $\Delta\sigma/2 = 380$ MPa, $N = 10^8$, (c) intergranular fatigue crack initiation due to high grain boundary normal stresses $\Delta\sigma/2 = 370$ MPa, $N = 10^9$, Tanaka-Mura-model [5] for (d) trans- and (e) intergranular fatigue crack initiation at slip bands, (f) EGM-model for intergranular fatigue crack initiation [15]

Pronounced extrusions and intrusions have been generated in the presented austenite grain, but no fatigue crack initiation in this or other austenite grains was observed. The latter was confirmed by means of FIB-cutting in combination with high-resolution SEM at several austenite grains with pronounced extrusions and intrusions. Figure 7c shows an example of such an investigation, in which a FIB-cut along the horizontal line in figure 7b was examined. No cracks were identified in the cross sections prepared. Hence, fatigue crack initiation at extrusion-intrusion-pairs, as proposed by Essmann, Gösele, Mughrabi [15] and Polák [16], seems to be of minor significance for the crack initiation process of the investigated duplex stainless steel subjected to loading amplitudes in the VHCF regime. The microstructure presented in figure 7b contains microcracks, which initiated transgranularly in a ferrite grain starting from intersection points between austenite slip traces and a phase boundary. Positions 1 to 4 show different stages of the transgranular microcrack initiation

process. Reaching the frictional shear stress in the austenite grain led to slip band formation on a $\{111\} \langle 110 \rangle$ slip system. The localized cyclic plastic deformation had to be endured by the surrounding grains, such as the neighboring ferrite grain. This induced stress intensifications, superimposed by elastic anisotropy stresses, and caused localized dislocation generation and motion in the neighboring ferrite grain (fig. 7b, pos. 1 and 2). A similar case is presented in figure 7d, which was taken from a TEM lamella prepared out of a run-out sample. Austenite slip bands caused very localized a high dislocation density in a neighboring ferrite grain because of stress intensifications at the tip of the slip bands. Cyclic irreversible motion of these dislocations on several parallel slip planes is correlated with the stage of fatigue crack initiation (fig. 7b, pos. 3 and 4). The crack nucleus in position 4 subsequently propagated alternating on several slip systems up to a length of about $6 \mu\text{m}$. Possible slip traces of $\{110\} \langle 111 \rangle$ slip systems according to crystallographic orientation data obtained by EBSD are plotted in circles. The stop of crack propagation in the midst of the first grain was probably due to a strong reduction of the shear stress amplitude at the crack tip during crack growth, which overcompensates the increase of the crack tip stress resulting from crack extension.

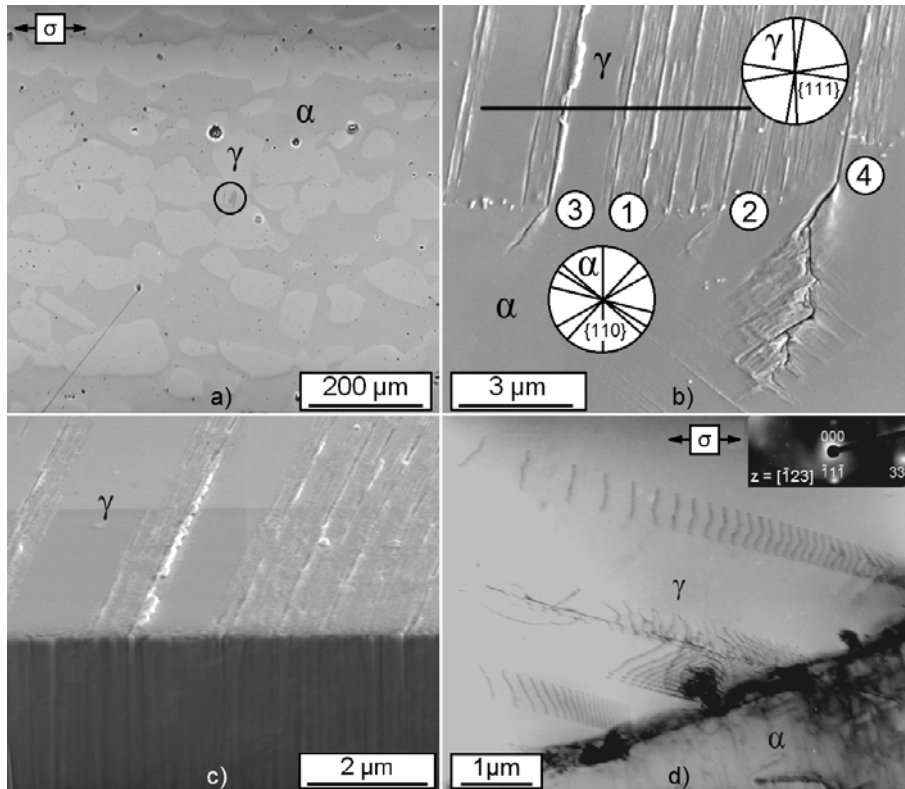


Fig. 7: (a) Surface of run-out sample ($\Delta\sigma/2 = 380$ MPa, $N = 10^9$), (b) detail image of area within circle in fig. 7a (possible slip traces are presented in circles), (c) inclined image of FIB-cut along horizontal line in fig. 7b and (d) TEM-image of austenite slip bands piling up against phase boundary causing dislocation generation and motion in the stress field at their tip in a neighboring ferrite grain ($\Delta\sigma/2 = 370$ MPa, $N = 10^9$)

3.4 Short fatigue crack propagation

The mechanisms of fatigue crack initiation and short crack propagation were investigated *in-situ* during fatigue experiments by means of an optical far field microscope. This enabled the determination of crack initiation sites and an analysis of the kinetics of short fatigue crack propagation. Figure 8a shows a fatigue crack which initiated at the phase boundary between the ferrite grain α_1 and the austenite grain γ_1 due to a high grain boundary normal stress caused by impinging slip bands in the austenite grain γ_1 . The fracture surface is presented in figure 8b, which shows the sample tilted by 45° . The brittle-fractured phase boundary is shown above the symbol γ_1 . The further fatigue crack propagation in the microstructure shown in figure 8b occurred transgranularly. The transition from intergranular fatigue crack propagation between the ferrite grain α_1 and the austenite grain γ_1 to

transgranular fatigue crack propagation through the ferrite grain α_1 caused a fanning of the crack. Zhai et al. [17] attribute this mechanism to a lower energy demand for fracturing the necessary small triangular grain boundary areas (fig. 8c) compared to the otherwise large triangular area. Thus, the crack forms steps by propagating on two different types of slip planes. Oscillating stripes on one of these slip planes is presented in higher magnification in the dashed rectangle. The kinematic analysis of the crack propagation, based on the data obtained by means of the far field microscope investigations, showed no barrier effect of the grain and phase boundaries shown in figures 8a and b in form of (i) deceleration, (ii) temporary stop or (iii) even permanent blocking of the fatigue crack.

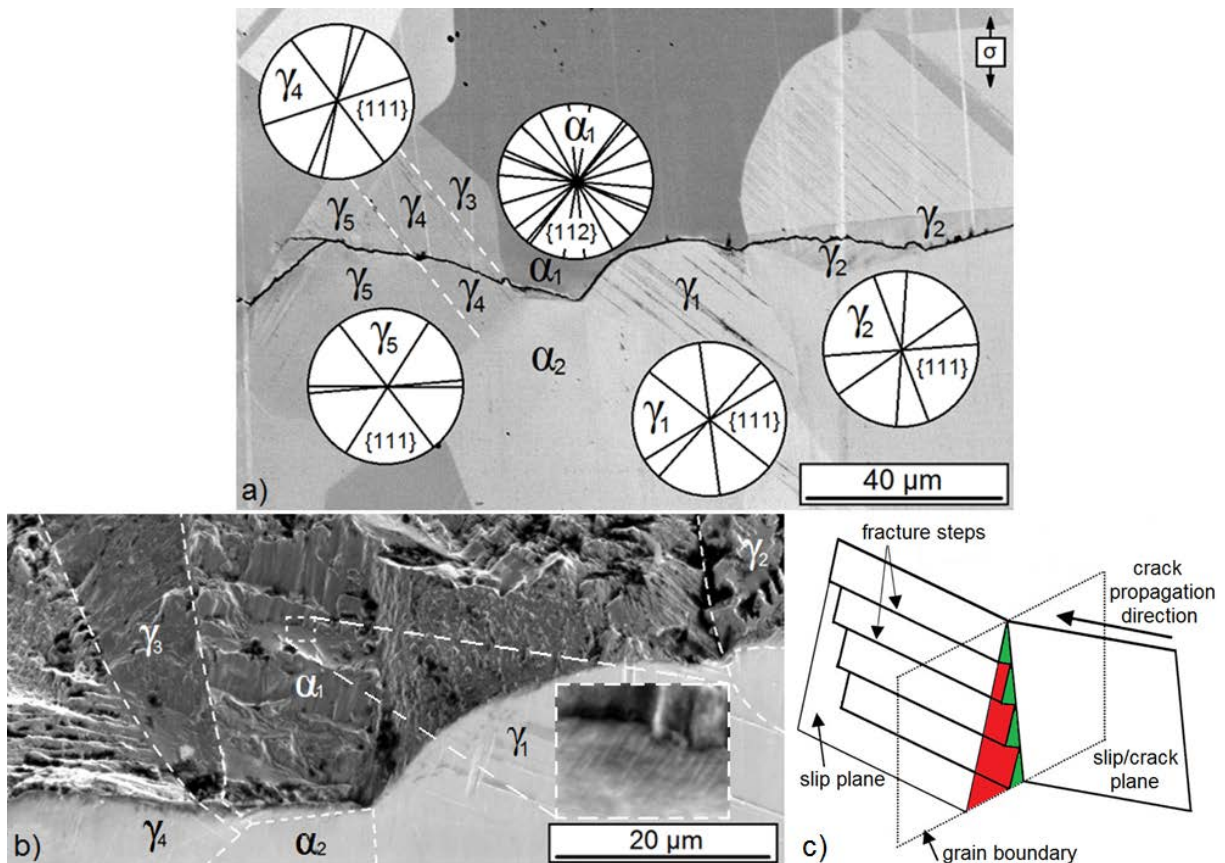


Fig. 8: Intergranular fatigue crack initiation site at phase boundary between the grains α_1 and γ_1 ($\Delta\sigma/2 = 370$ MPa, $N_f = 2.18 \cdot 10^6$): (a) electron channeling contrast image of sample surface (circles show possible slip traces), (b) secondary electron image of sample surface and fracture surface and (c) fractured grain boundary area showing schematically fanned (red) or not fanned crack transfer (red + green) [17]

Only 2 out of 7 fatigue cracks were temporarily arrested by phase boundaries. 7 cracks in 22 run-out samples were permanently blocked by phase boundaries (2 at the first phase boundary and 5 at later phase boundaries) at least until the ultimate number of loading cycles of 10^9 have been reached. 28 samples failed by a fatal fatigue crack. These cracks could not be blocked permanently by grain or phase boundaries. 35 microcracks in 22 run-out samples did not reach the first grain or phase boundary. With a few exceptions, the experimental results show that a microstructure of the investigated duplex stainless steel fails under high and very high cycle fatigue conditions when at least one crack is able to reach or overcome the first microstructural barrier (grain or phase boundary).

3.5 High-energy X-ray diffraction investigations

The results of the X-ray diffraction measurements have shown two distinct effects. The first effect was a broadening of selected austenite peaks with increasing numbers of load cycles. The broadening was attributed to the increase of dislocation density in the austenite phase due to cyclic loading. The other effect was a small drift of most of the ferrite peaks and some austenite peaks in the radial direction of the 2D-detector as a function of load cycles, which can be described as changes of respective lattice parameters due to the generation of residual stresses during the fatigue process.

Due to the random orientation of the grains with respect to the incident beam, Debye-Scherrer-like diffraction patterns appeared at the detector where the ring diameters corresponds to different Bragg angles 2θ . A typical line profile of the diffraction intensity is shown in figure 9 obtained after integration of the ring intensity over an azimuth angle of 4 degrees.

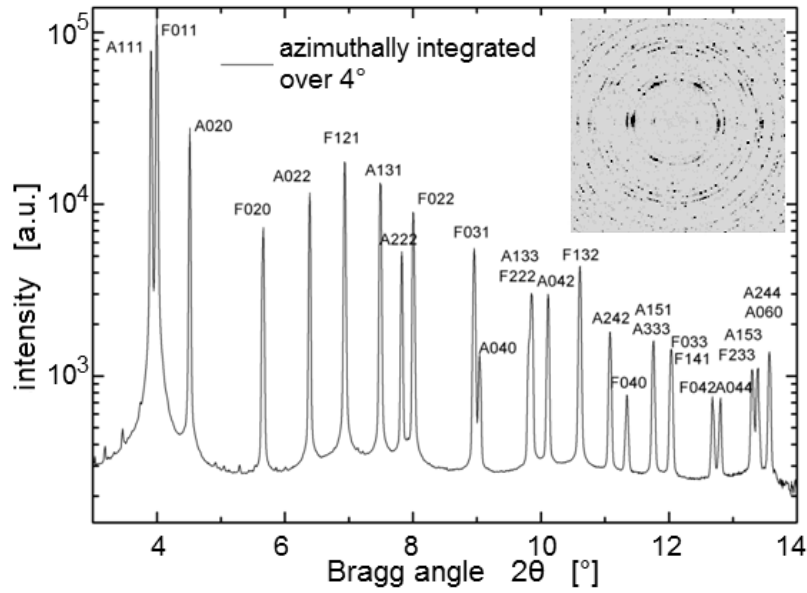


Fig. 9: Azimuthally integrated diffraction pattern (over 4°) comprising a large number of diffraction spots from distinct grains (see the inset); Small shifts of austenite $\{040\}$ and ferrite $\{031\}$ reflections having similar Q values were later used for investigation of individual grains by choosing and analyzing isolated diffraction spots on the 2D-pattern, each of them corresponding to a single grain

The 2D diffraction patterns on the detector showed a large number of spatially well-resolved Bragg peaks. Because of the relative small number of grains fulfilling the Bragg condition at the same time, the Debye-Scherrer rings split into a large number of individual spots. By sorting 2θ , each spot can be identified as either austenite or ferrite Bragg peak and indexed according to its radial position. Each of the visible spots can be attributed to diffraction of a single grain satisfying the Bragg condition. Therefore the experiment allows for a single-grain analysis. A plot equivalent to the rocking curve (RC), i.e. the intensity distribution as function of the Bragg angle θ of a given grain, can be obtained by plotting the spot intensity from patterns taken at different rotation angles Ψ , where the grain specific incident Bragg angle θ can be calculated from the rotation angle Ψ and the angle between the normal of measured lattice plane reflection and the axis of rotation. Thus, the best resolution in terms of the angle θ is obtained for the reflections lying close to the load axis, whereas for the reflections perpendicular to the load axis the resolution of the θ angle is close to the minimum rotation angle used, Ψ (0.05°). On the other hand, the radial position of each Bragg reflection can be fitted as well, which gives a value of the lattice parameter a for the respective austenite or ferrite grain.

Thus, the evolution of RCs widths and the lattice parameters for a large number of grains were measured as a function of load cycles.

Figure 10 shows a typical broadening of one of the austenite {131} reflections in terms of an increasing Bragg angle width θ as a function of load cycles. The RCs shown in figure 10a were fitted using the pseudo-Voigt function. The corresponding widths from the fits are shown in figure 10b (left scale). The relatively large error bars result basically from irregular shapes of the respective RCs. A dislocation density approximation (right scale in figure 10b) can be calculated using Hirsch's approximation [18]. It was found that the width of RCs increases gradually with the number of load cycles up to approximately 10^7 load cycles and then stabilizes. This behaviour is remarkably similar to the broadening of the roughness profile of the slip trace agglomerate in figure 5b.

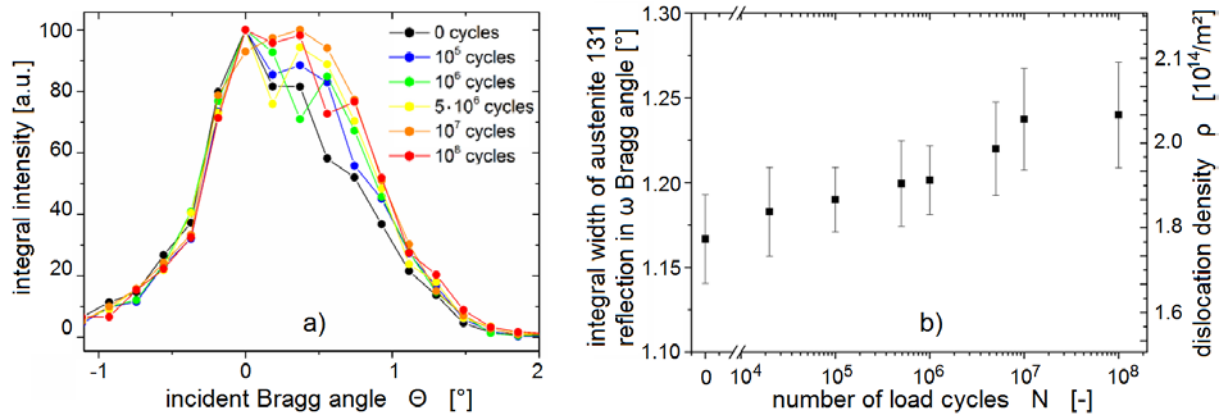


Fig. 10: (a) RCs of an austenite {131} reflection for various load cycles and (b) fitted width of the same reflection as a function of the incident Bragg angle (left scale) and dislocation density estimation as a function of the number of load cycles (right scale)

Both effects (broadening of RCs in Bragg case and development of slip traces) were related to the generation of slip bands in the austenite phase, which consist of edge dislocations.

Additionally to RC measurements, the changes of lattice parameters of 10 austenite {040} and 25 ferrite {031} reflections were analyzed as a function of load cycles. In order to determine the mean peak position $2\theta(hkl)$ the intensities of each of those reflections were azimuthally integrated along the Debye-Scherrer ring and fitted with pseudo-Voigt functions before the fatigue experiment as well as

after every fatigue interval. Subsequently the corresponding Bragg angles $2\theta(hkl)$ and resulting individual d-values $d(hkl)$ and respective lattice parameters $a=d(hkl)(h^2+k^2+l^2)^{1/2}$ for each grain were determined. The relative changes of the lattice parameters ($\Delta a/a$) with respect to the unfatigued sample were analyzed as a function of the number of load cycles. It was found that the behaviour of all analyzed grains could be qualitatively divided into 3 distinct cases (see fig. 11).

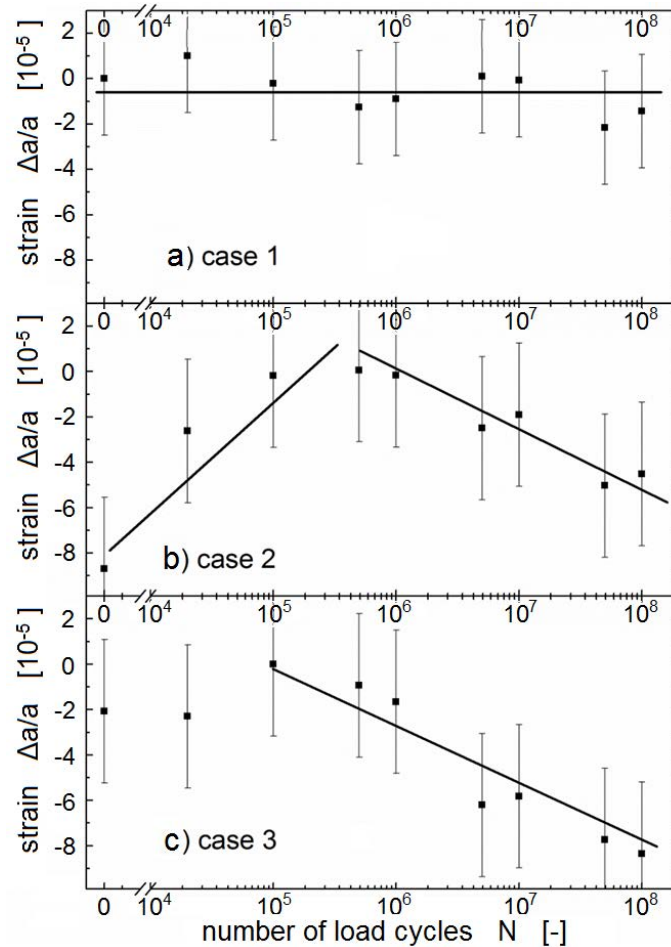


Fig. 11: Three distinct cases of strain development in individual austenite and ferrite grains: (a) case 1: an austenite {040} reflection - no visible change with increasing number of load cycles, (b) case 2: a ferrite {031} reflection - initial relief of compressive strain up to about $5 \cdot 10^5$ load cycles and subsequent development of secondary strain at higher number of load cycles and (c) case 3: another ferrite {031} reflection - gradual increase of compressive strain with increasing number of load cycles (obvious trends are shown in solid lines)

The first case comprises 7 out of 10 investigated austenite grains and 7 out of 25 ferrite grains, where only small fluctuations of the lattice parameter (around 0.002%) were found. In the second case a relief of initial compressive strain was found in 14 ferrite grains until about $5 \cdot 10^5$ load cycles accompanied by a development of secondary strain at higher numbers of load cycles. The third case was observed in 4 ferrite and 3 austenite grains, being a gradual development of compressive strain with increasing number of load cycles.

3.6 Simulation of fatigue damage evolution

Figure 12a shows a three dimensional finite element model consisting of tetrahedral elements. The nodes at its left side are fixed in x-direction, whereas the nodes at its right side are monotonically loaded by forces in x-direction leading to a normal stress of $\sigma=350$ MPa. The material behaviour was defined as isotropic elastic ($E = 197$ GPa). The model contains an austenite slip band (red elements) with a Schmid factor of 0.5, a slip direction lying in the model surface (top face in fig. 12a) and a slip trace lying 45° to the x-axis. The element mesh is refined at and close to the austenite slip band. By means of a modified user material subroutine (UMAT) (originally developed by Huang [19]), the elements of the austenite slip band execute a plastic shear strain when the frictional shear stress of the austenite phase is reached ($\tau_{fr}=68$ MPa). Figure 12b shows the normal stress distribution in the cross section A-A (see fig. 12a), which represents a grain boundary or a phase boundary.

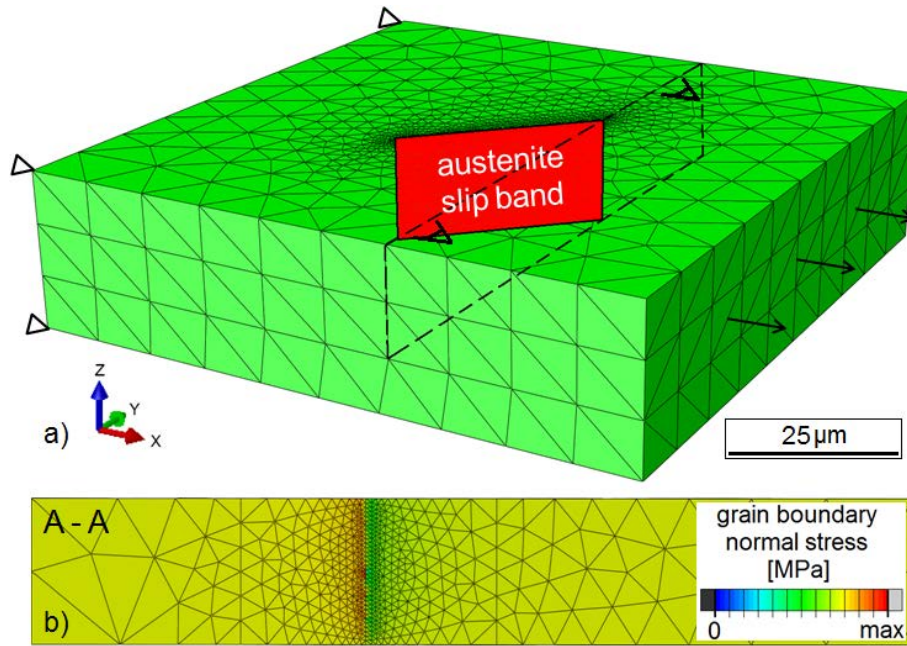


Fig. 12: (a) 3D finite element model containing an austenite slip band (red) and (b) normal stress distribution in cross section A-A (see fig. 12a) representing a grain boundary or a phase boundary,

$$\sigma = 350 \text{ MPa}$$

The plastic shear strain of the slip band elements, which develops when the frictional shear stress is reached, caused stress intensifications at the grain or phase boundary at the intersection line between the slip band and the boundary (red area in the fine-meshed region in fig. 12b). Such stress intensifications are correlated with the stage of intergranular fatigue crack initiation as described in section 3.3.

Figure 13a shows a three dimensional finite element model consisting of tetrahedral elements. The nodes at its left face are fixed in x-direction, whereas the nodes at its right face are cyclically loaded by forces in x-direction leading to a stress amplitude of $\Delta\sigma/2=350 \text{ MPa}$. The material behaviour was defined as elastically isotropic ($E=197 \text{ GPa}$). The model contains an austenite grain (yellow cuboid) and an austenite slip band (red elements) with a Schmid factor of 0.5, a slip direction laying in the model surface (top face in Fig. 13a) and a slip trace laying at 45° to the x-axis. The element mesh is refined at and close to the slip band. The elements of the austenite slip band can perform plastic shear strain when the frictional shear stress of the austenite phase is reached ($\tau_{fr}=68 \text{ MPa}$). There is an additional ferrite grain (blue cuboid) and a ferrite slip band (red elements)

beside the austenite slip band with a frictional shear stress of $\tau_{fr}=99$ MPa. For the sake of visualization, the ferrite slip band is tilted and twisted by 10° regarding the austenite slip band, respectively, which causes a Schmid factor of 0.46.

Equation 1 and 2 show the relationship between the number of load cycles for fatigue crack initiation and the range of the plastic shear strain. Hence, the cyclically accumulated squared shear strain range is used as fatigue damage parameter FDP for simulating the processes of crack initiation and short crack propagation (Eq. 5).

$$FDP = \sum_{N=1}^N \Delta\gamma_{pl}^2 \quad (5)$$

The elements of the ferrite slip band in figure 13 lose their stiffness and behave like a crack element once a critical value of the fatigue damage parameter FDP is reached. A fatigue crack nucleus is formed when the critical value of this parameter is reached in the first element. The subsequent short fatigue crack propagation is assumed to be a consequence of fatigue damage of neighboring elements.

Equation 5 presents a well known short fatigue crack propagation law [20] based on the range of the crack tip slide displacement $\Delta CTSD$, the coefficient C and the exponent m .

$$\frac{da}{dN} = C \cdot \Delta CTSD^m \quad (5)$$

$\Delta CTSD$ is caused by the shear strain range $\Delta\gamma_{pl}$ at the crack tip and thus these quantities can be assumed to be proportional to each other. By means of experimental and numerical investigations of the same duplex steel, Düber et al. [9] determined the exponent m to be about 1, so that there is a proportionality between da/dN and $\Delta CTSD$. In the present study, this proportionality between $\Delta\gamma_{pl}$ and da/dN was also found by applying the above mentioned fatigue damage criterion.

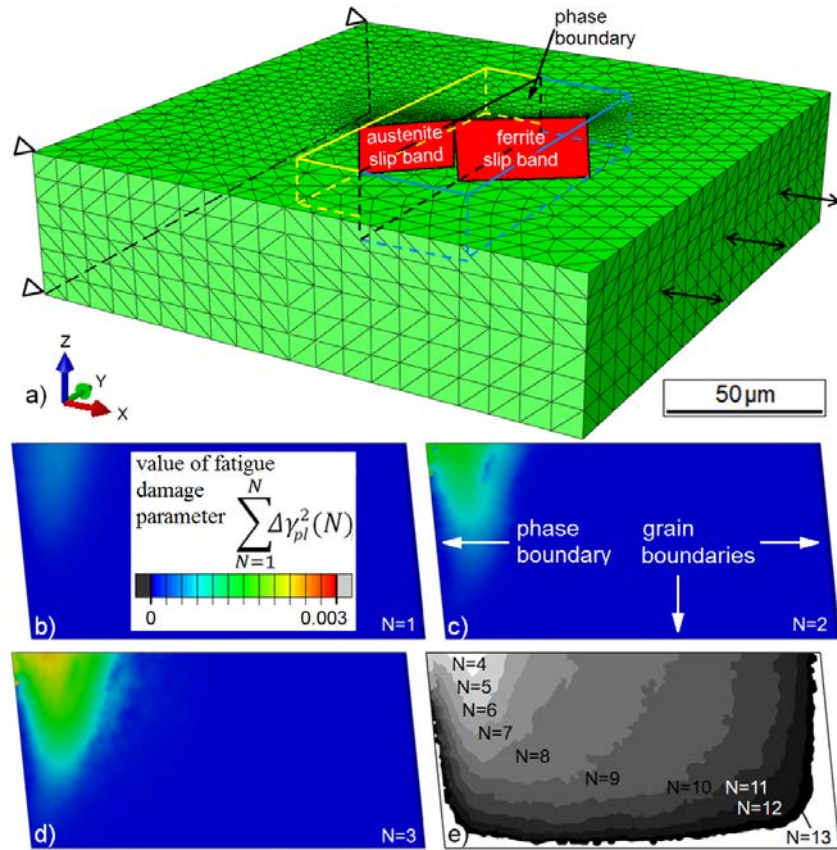


Fig. 13: (a) Elastically isotropic 3D finite element model containing an austenite grain (yellow cuboid) and a ferrite grain (blue cuboid); (b) distribution of the damage parameter value in the ferrite slip band after one simulated load cycle, (c) after two simulated load cycles, (d) after three simulated load cycles and (e) progress of crack front for four to thirteen simulated load cycles, $\Delta\sigma/2=350$ MPa, critical value of the damage parameter=0.003 (arbitrarily chosen)

The derivation of the fatigue damage criterion shows that transgranular microcrack initiation and short fatigue crack propagation are related to the same basic mechanisms, namely the irreversible fraction of cyclic dislocation motion. Figures 13b to c show the distribution of the damage parameter value on the plane of the ferrite slip band after the first, second and third simulated load cycle. Figure 13d shows in which areas the critical value of 0.003 (arbitrarily chosen) is reached on the plane of the ferrite slip band after the 4th to 13th simulated load cycle. The elements in the presented areas lost their stiffness and form a crack. This caused stress intensifications at the crack tip, which accelerated the crack propagation in the sample surface (x-y-plane) as well as in the sample depth (z-direction). The increase in crack propagation rate is documented by the increasing distances between

the crack fronts. Successively, the crack was converging to the grain or phase boundaries at the lower and right side in figure 13e. This caused a decrease of the remaining slip band length and thereby a decrease of the plastic shear strain range at the crack tip, which is the driving force for short fatigue crack propagation.

Anisotropic elasticity and residual stresses resulting from the heat treatment of the duplex stainless steel, cause a heterogeneous stress distribution in the single grains. Fatigue cracks, which initiate in regions of maximum stress, thus generally grow into regions with lower stress. This can cause a decrease of the plastic shear strain range at the crack tip and thereby can lead to a deceleration or stop of short fatigue crack propagation. The presented model is able to predict in a mechanism-based manner the fatigue life of real microstructures of the investigated duplex stainless steel. The microstructure can be obtained by means of automated EBSD (2D grain shapes) or phase and diffraction contrast tomography (PCT / DCT) in experiments using synchrotron radiation (3D grain shapes) [21]. By additionally considering anisotropic elasticity and residual stresses, the model developed enables the prediction whether microcracks (i) initiate in a given microstructure, (ii) arrest in the midst of the first grain, (iii) are permanently, (iv) temporary or (v) not at all blocked by grain or phase boundaries.

4. Conclusions

Very high cycle fatigue tests up to one billion load cycles at amplitudes close to the fatigue limit showed that slip band generation in an austenitic-ferritic duplex stainless steel (318 LN) almost completely takes place in few austenite grains without any microcrack initiation in these grains.

Cyclic plastic deformation within single austenite slip bands strongly reduces during a relatively low number of load cycles after slip band generation ($\Delta N < 10^5$), indicating a relatively strong cyclic hardening of the austenite phase. The hardening can cause a shifting of plastic deformation into neighboring areas accompanied by an increase of the slip band density until very high numbers of load cycles ($10^5 < N < 10^8$). Subsequently the slip band density remains almost constant ($10^8 < N < 10^9$).

Fatigue cracks under such loading conditions most frequently initiate at or close to phase boundaries. That is due to stress intensifications caused by impinging austenite slip bands, which are superimposed by elastic anisotropy stresses. These stress intensifications can cause dislocation generation in neighboring ferrite grains close to phase boundaries. The irreversible fraction of motion of such dislocations on several parallel slip planes is correlated with the stage of fatigue crack initiation. As a second mechanism, these stress intensifications can cause high phase boundary normal stresses, which can lead to a brittle-type fracture of the phase boundary.

Fatigue experiments in laboratory air atmosphere as well as in vacuum clearly showed that an increased irreversibility of cyclic plastic slip (in air) accelerates the microstructural damage evolution and thus decreases fatigue life.

The mechanisms of slip band formation, microcrack initiation and short fatigue crack propagation were implemented into three-dimensional finite element simulations, which consider crystal plasticity. The simulations are able to determine under which conditions microcracks (i) initiate, (ii) arrest in the midst of the first grain, (iii) are permanently, (iv) temporary or (v) not at all blocked by grain or phase boundaries. This provides a mechanism-based life prediction methodology which can be applied to real microstructures determined by means of automated EBSD (2D grain shapes) or phase and diffraction contrast tomography (PCT / DCT) experiments (3D grain shapes). Moreover, such simulations can contribute to the concept of tailored microstructures for improved resistance to VHCF conditions.

Acknowledgement

The authors would like to thank Deutsche Forschungsgemeinschaft (DFG) for financial support in the framework of the priority program “life[∞]” (SPP1466).

References

- [1] T. Sakai, Review and prospects for current studies on very high cycle fatigue of metallic materials for machine structural use, *J. Solid Mech. Mater. Eng.* 3 (2009) 425-439.

- [2] Y. Murakami, M. Endo, Effects of defects, inclusions and inhomogeneities on fatigue strength, *Int. J. Fatigue* 16 (1994) 163-182.
- [3] I. Roth, M. Kübbeler, U. Krupp, H.J. Christ, C.P. Fritzen, Crack initiation and short crack growth in metastable austenitic stainless steel in the high cycle fatigue regime, *Proc. Eng.* 2 (2010) 931-940.
- [4] U. Krupp, H. Knobbe, H.J. Christ, P. Köster, C.P. Fritzen, The significance of microstructural barriers during fatigue of a duplex steel in the high-and very-high-cycle-fatigue (HCF/VHCF) regime, *Int. J. Fatigue* 32 (2010) 914-920.
- [5] K. Tanaka, T. Mura, A dislocation model for fatigue crack initiation, *J. Applied Mech.* 48 (1981) 97-103.
- [6] A. Wilkinson, S.G. Roberts, A dislocation model for the two critical stress intensities required for threshold fatigue crack propagation, *Scripta Mater* 35 (1996) 1365-1371.
- [7] E.O. Hall, The Deformation and Ageing of Mild Steel: III Discussion of Results, *Proc. of the Royal Society* 64B (1951) 747-753.
- [8] N.J. Petch, The cleavage strength of polycrystals, *J. Iron and Steel Inst.* 174 (1953) 25-28.
- [9] O. Düber, B. Künkler, U. Krupp, H.J. Christ, C.P. Fritzen, Experimental characterization and two-dimensional simulation of short-crack propagation in an austenitic–ferritic duplex steel, *Int. J. Fatigue* 28 (2006) 983-992.
- [10] K. Istomin, B. Dönges, N. Schell, H.J. Christ, U. Pietsch, Analysis of VHCF damage in a duplex stainless steel using hard X-ray diffraction techniques, *Int. J. Fatigue* 66 (2014) 177-182.
- [11] R. Wang, H. Mughrabi, S. McGovern, M. Rapp, Fatigue of copper single crystals in vacuum and in air I: Persistent slip bands and dislocation microstructures, *Mater. Sci. and Eng.* 65 (1984) 219-233.
- [12] R. Wang, H. Mughrabi, Fatigue of copper single crystals in vacuum and in air II: Fatigue crack propagation, *Mater. Sci. and Eng.* 65 (1984) 235-243.
- [13] N.M. Gringberg, The effect of vacuum on fatigue crack growth, *Int. J. Fatigue* 4 (1982) 83-95.

- [14] K.S. Chan, A microstructure-based fatigue-crack-initiation model, *Metallurgical and Materials Transactions A* 34A (2003) 43-58.
- [15] U. Essmann, U. Gösele, H. Mughrabi, A model of extrusions and intrusions in fatigued metals I. Point-defect production and the growth of extrusions, *Phil. Mag. A* 44 (1981) 405-426.
- [16] J. Polák, On the role of point defects in fatigue crack initiation, *Mater. Sci. Eng.* 92 (1987) 71-80.
- [17] T. Zhai, A.J. Wilkinson, J.W. Martin, A crystallographic mechanism for fatigue crack propagation through grain boundaries, *Acta Mater.* 48 (2000) 4917-4927.
- [18] A. Fingerland, *Acta Cryst. A* 27 (1971) 280-284
- [19] Y. Huang, A User-Material Subroutine Incorporating Single Crystal Plasticity in the Abaqus Finite Element Program, Harvard University, Division of Applied Sciences, 1991.
- [20] K. Tanaka, Y. Akinawa, Y. Nakai, R.P. Wei, Modelling of small fatigue crack growth interacting with grain boundary, *Eng. Fract. Mech.* 24 (1986) 803-819
- [21] W. Ludwig, J.Y. Buffière, S. Savelli, P. Cloetens, Study of the interaction of a short fatigue crack with grain boundaries in a cast Al alloy using X-ray microtomography, *Acta Mater.* 51 (2003) 585-598.